Gas transport in a binary bentonite mixture used in sealing systems

Arisleidy Mesa-Alcantara[1*], *Enrique* Romero[1,2] and *Nadia* Mokni[3]

[1] International Centre for Numerical Methods in Engineering CIMNE, 08034 Barcelona, Spain
[2]Universitat Politècnica de Catalunya UPC, 08034 Barcelona, Spain
[3]Institut de Radioprotection et de Sûreté Nucléaire IRSN, 92260 Fontenay-aux-Roses, France

Abstract. Binary mixtures composed of 80% of high-density pellets and 20% of granular bentonite at hygroscopic water content are currently considered for use in vertical sealing systems for the deep and long-term disposal of radioactive wastes. By pouring the dry components without compaction, the mixture displays a dry density of around 1.49 Mg/m^3. However, these sealing systems are subjected to long-term hydrations from the surrounding formations with the possibility of having zones with entrapped and generated gas that makes it challenging to display a homogeneous saturation of the seal. Therefore, gas transport through these bentonite-based sealing materials at different degrees of saturation is a crucial issue. Hence, several oedometer tests have been conducted to evaluate the impact of gas injection on this mixture at different degrees of saturation and constant pouring dry density. These gas injection/dissipation tests were performed at constant vertical stress or constant volume conditions. The results provided the variation of the effective gas permeability at different degrees of saturation and the gas breakthrough pressure after saturation. Furthermore, these gas transport results were interpreted with a microstructural study of the mixture focusing on the volumetric filling of the inter-pellet porosity.

1 Introduction

Binary bentonite-based mixtures with a shielding skeleton of high-density pellets (80% in mass) and granular bentonite partially filling the voids form a material with a dry density of around 1.49 Mg/m^3 on pouring, which has been recently considered in vertical sealing systems for the deep and long-term disposal of radioactive wastes [1,2]. The French Institute for Radiological Protection and Nuclear Safety (IRSN) has been recently involved in the 'Vertical Sealing System' (VSEAL) project that studies the long-term hydration process of this engineered barrier system and the impact of gas transport at different hydraulic states. Once installed, this sealing material will be affected by coupled hydro-mechanical processes and gas transport: a) hydration under constant volume due to water infiltration from the geological barrier (faster at the top and slower on lateral hydration) and the corresponding increase in swelling pressure; and b) gas entrapment and pressurisation at long term induced by several processes (anaerobic corrosion of metallic canisters, microbial degradation of organic substances, radiolysis of water). Furthermore, in scenarios where the gas production rate exceeds the rate of gas diffusion in the pore water, gas will build up and can induce local overpressure on the engineered barrier [3], generating other transport mechanisms, such as two-phase flow and dilatancy-controlled gas flow through local pathways and interfaces [4].

This heterogeneous mixture presents a multi-modal pore network that evolves during hydration, which will have consequences on the short-term HM behaviour of the material and its long-term response to gas transport. It is, therefore, essential to understanding these microstructural features when assessing the gas transport properties at different hydraulic states.

This paper presents gas injection/dissipation tests performed on the bentonite-based mixture at different degrees of saturation. The experiments are carried out under oedometer conditions. Effective gas permeability, a measure of the ability of gas to flow in the presence of a water phase (product of the relative permeability and the intrinsic permeability), has been evaluated. Tests at full saturation are also devoted to estimating the gas breakthrough pressure. The gas transport tests are complemented with a microstructural study and compared with published sand/bentonite mixtures data.

2 Material

MX-80 type bentonite, the base material of the pellet/powder mixture, has a high montmorillonite content (80%), liquid limit 420-560%, plastic limit 62%, and density of particles 2.77 Mg/m^3 [5]. High-density bentonite pellets (around 7 mm diameter) have been uniaxially compacted (Laviosa-MPC, France) to reach a

* Corresponding author: arisleidy.mesa@upc.edu

dry density of 1.99-2.12 Mg/m^3. The powder (granular bentonite) is fabricated by crushing pellets with a maximum particle size of 2 mm and a poured dry density of around 1.10 Mg/m^3 [6,7]. Binary mixtures of 80% high-density pellets and 20% granular bentonite are prepared for the study (Figure 1). The mixture presents a dry density of 1.49 Mg/m^3 at an initial water content of w=7.90%, corresponding to a void ratio e=0.859 and an initial degree of saturation S_r=25.5%.

The samples are prepared directly into the 50 mm diameter cell placing the pellets one by one to ensure a coordination number close to eight and then adding the corresponding amount of powder. The samples display two layers of pellets (37 pellets per layer), reaching a height of 14 mm. A sample with three layers of pellets and a height of 21 mm is also prepared for the oedometer test under full saturation conditions.

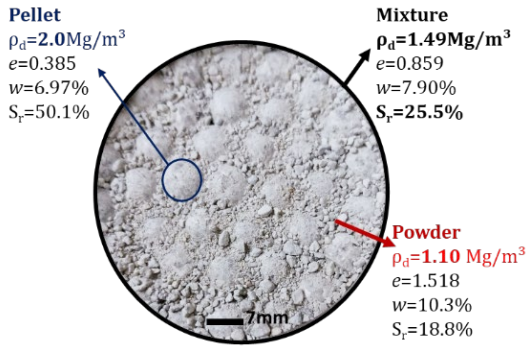

Fig. 1. Bentonite mixture of 80% pellets and 20% powder.

Figure 2 shows the results obtained by mercury intrusion porosimetry (MIP) of the pellet and the powder at their initial state. Bimodal pore size distributions are observed for both components. The intruded void ratio of the pellet is 0.36, which represents 92% of its total void ratio (e=0.39) (Figure 2a). This deviation is due to the limited capacity of the porosimeter to enter the smallest pores (non-intruded void ratio with entrance pore sizes below 7 nm). On the other hand, the intruded void ratio of the powder (e_{int}=0.88) is lower than its total void ratio (e=1.52), indicating mainly the non-detected void ratio with pore sizes larger than 400 µm.

A value of 1 µm was considered to separate these two pore domains in the pellet and powder [8]. Figure 2b shows a pellet and powder's pore size distribution (PSD). As observed, pellet and powder display the smaller dominant entrance pore size at approximately 20 nm. The pellet displays the largest dominant pore mode between 10 µm and 20 µm. However, the powder shows the most significant dominant pore mode between 170 µm and 190 µm. Consequently, the mixture displays a multi-modal pore network with microporosity (intra-aggregate pores in powder and pellets), macroporosity (inter-aggregate pores in powder and pellets), and larger macropores between the shielding skeleton of the pellets and the powder (inter-grain porosity considered hereafter as part of the macro-porosity)[9].

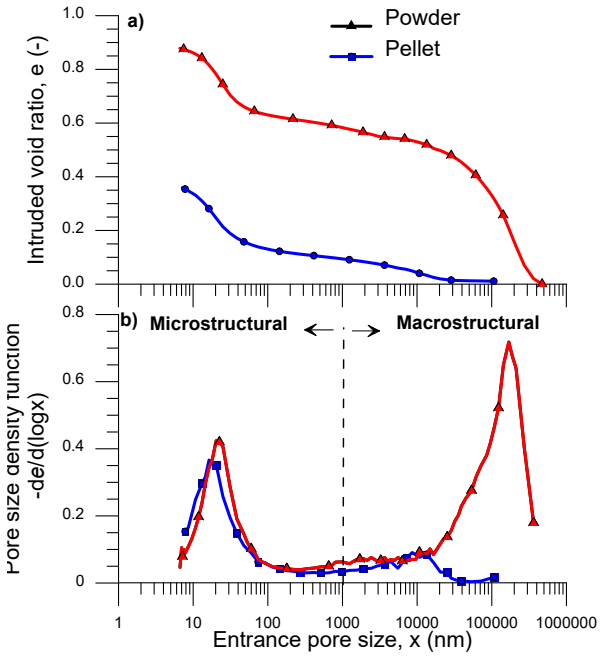

Fig. 2. a) Cumulative intruded void ratio and b) PSD for a pellet and powder at the initial state.

3 Experimental setup and tests protocols

3.1 Experimental setup

Several gas injection/dissipation tests were performed at different degrees of saturation. Dry air was used as the injection gas. The tests were carried out at constant total vertical stress or constant volume in a high-stress oedometer cell [10]. The setup of the gas dissipation test at constant injection gas volume and the auxiliary devices are presented in Figure 3. A small stiff load cell with a range of 20 kN and accuracy <0.2%FS is used to determine the total vertical stress (constant volume test). Two automatic pressure/volume controllers inject gas and water at the bottom of the sample.

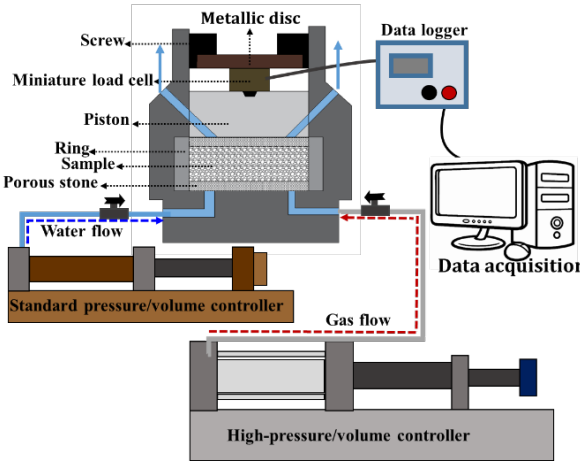

Fig. 3. Setup of the gas dissipation test.

3.2 Experimental protocols on the saturated mixture

Table 1 summarises the conditions of the samples before gas injection. Tests 3, 4 and 5 under constant volume are described in section 3.2.

In the case of Test 2, the sample was previously saturated under isochoric conditions for more than 300 days before the gas injection. This saturated test aims at determining the breakthrough pressure, followed by gas dissipation.

Table 1. State of the different samples before gas injection.

Sample	Dry density (Mg/m^3)	Degree of saturation (%)	Type of tests (oedometer)
Test 1	1.55	27.7	Constant total stress
Test 2	1.49	100	
Test 3	1.49	25.5	Constant volume
Test 4		82.8	
Test 5		89.6	

Following a strict protocol (summarised in Figure 4) is crucial in the case of the saturated sample (Test 2), which developed a high swelling pressure of around 3.3 MPa during the long-term hydration. The protocol starts with an unloading step from the isochoric test that involves generating high matric suction even when the material is saturated. The different stages followed in Test 2 are described below.

Stage 1. Pre-conditioning path: The total vertical stress is increased at a rate of 15 kPa/min until a value of 4 MPa, keeping the samples' top and bottom caps filled with air under atmospheric conditions. The total vertical stress of 4 MPa induces the matric suction - generated on unloading- to decrease (Figure 4a).

Stage 2. Water permeability determination: The top and bottom caps are filled with distilled water. Since no appreciable matric suction remains, the sample does not undergo a significant volume change (only osmotic suction plays some role). The saturated water permeability is determined under steady-state conditions. The water pressure at the bottom and the top of the sample is kept at 0.5 and 1 MPa, respectively (Figure 4b). During this stage, the sample expanded due to vertical effective stress decrease, which changed from 4 MPa (at the end of the compression) to a mean value of 3.25 MPa under steady-state flow conditions.

Stage 3. Drainage of the bottom cap: The water pressure in the bottom vessel is quickly reduced until reaching atmospheric conditions, which allows water replacement by gas (Figure 4c).

Stage 4. Gas injection: The maximum gas (air) pressure is limited to 1.5 MPa to avoid exceeding the total radial stress. This total radial stress is estimated at around 3.5 MPa at the end of the previous stage ($K_0 \approx 0.86$ for an estimated friction angle of $\phi' = 8°$). Therefore, a minimum of 1 MPa can be accepted as the difference between total vertical stress and maximum gas pressure to avoid preferential gas flows between the sample and the oedometer ring [11].

Gas injection is applied at the bottom of the sample in four fast injection pressure ramps (Figure 4d). The injection piston is shut-off at each step of the gas pressure, and it is allowed to decay at a constant gas volume of the inlet line. The gas pressure is maintained stable during the first three steps, indicating no breakthrough or gas pathway through the sample. Nevertheless, a pressure drop was observed in the last injection pressure step.

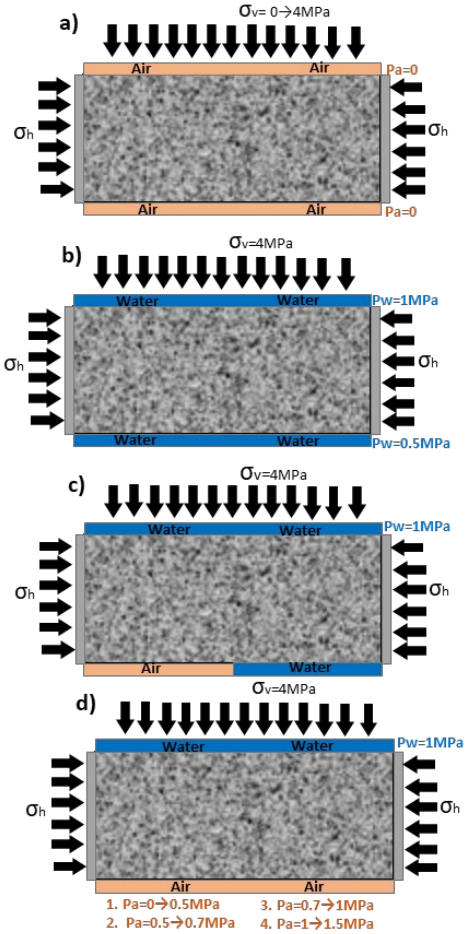

Fig. 4. Schematic of test protocols followed (Test 2): a) Pre-conditioning path, b) water permeability determination, c) drainage of the bottom cap and d) gas injection at a maximum pressure of 1.5 MPa.

3.3 Constant volume protocols on unsaturated mixtures

Three gas dissipation tests (Tests 3, 4 and 5) under constant volume conditions were run with the protocol described below. Test 3 was accomplished at the initial state (S_r=27.7%), while the remaining were performed at higher saturations (Table 1).

Stage 1. Pre-conditioning path: Vertical total stress of around 1.0 MPa is applied to the samples. Afterwards, the loading system is blocked to ensure constant volume conditions (a load cell allows determining the initial total vertical stress).

Stage 2. Hydration path: The samples are saturated until reaching different degrees of saturation. Water is supplied to the samples by applying a water pressure of

20 kPa at the bottom boundary for a short period. The valve is closed once the target amount of water is reached. The load cell allows for registering the time evolution of total vertical stress (swelling pressure).

Stage 3. Gas injection: Gas pressure is limited to 1.0 MPa. The gas pressure is applied when no change in the swelling pressure is observed (Test 4 and 5). After the injection pressure, the piston is closed (shut-off at constant injection volume). Test 1 at constant vertical stress was performed by applying a fast gas injection pressure of 1 MPa.

4 Test results and interpretation

4.1 Calculation of the effective permeability

The product between the relative permeability to air and the intrinsic permeability defines the effective permeability (K_{eff}). K_{eff} was estimated using the gas pressure decay method according to the following equation:

$$K_{eff} = -\frac{2\mu_g L V_1}{A(P_1^2 - P_2^2)}\frac{dP_1}{dt} \quad (1)$$

where V_1 is the volume of the pressurised upstream reservoir (5×10^{-3} m^3) (dead and piston volumes), A is the sample cross-sectional area, L is the height of the sample, P_1 is the absolute gas pressure at the inlet, P_2 is the absolute atmospheric pressure at the outlet, and μ_g is the gas (air) dynamic viscosity (1.81×10^{-5} Pa.s) at 20°C and 101 kPa.

4.2 Oedometer results at constant vertical stress

Figure 5 shows the evolution of outflow volume, axial displacement, outflow pressure and injection pressure for the saturated sample (Test 2) at a constant total vertical stress of 4 MPa. The injection pressure at the bottom boundary (injection point) increased in time following the four injection pressure steps (from A to D in Figure 5). After each pressure increment, the injection piston was closed (shut-off at constant injection volume). These injection pressure steps progressively decreased the effective vertical stress because of increased pore pressure. At 1.5 MPa, the cumulative axial strain was close to -1% (negative values represent expansive behaviour). At this high pressure and after 1.5 days from the beginning of the stage, the injection pressure decreased, and the outflow volume increased. This fact indicated a 'soft breakthrough pressure' with the opening of a gas pathway at a gas pressure of 1.5 MPa. The concept of 'soft breakthrough' has been introduced to indicate that the passage was created following some time after the gas pressure increase. The effective gas permeability (considering the complete cross-section) was determined during the dissipation stage. After dismantling, a fissure was observed in the central part of the sample, indicating that the gas pathway developed inside the sample.

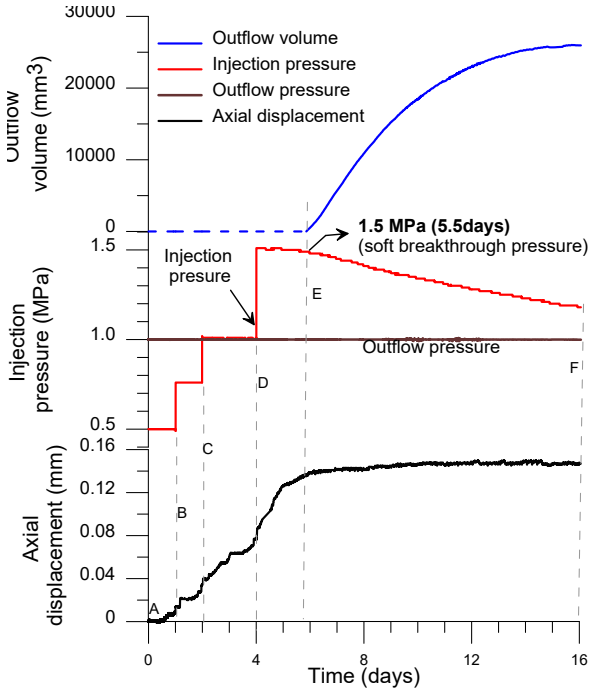

Fig. 5. Time evolution of injection pressures, outflow volume, outflow pressure and axial displacements (expansion of the sample) at a constant vertical stress of 4 MPa.

4.3 Oedometer results under constant volume

Test 4 reached a value of total vertical stress (swelling pressure) of 1.45 MPa after almost seven days, and Test 5 reached 1.90 MPa after five days of hydration (Figure 6). The stress evolution of Tests 4 and 5 presents features that different authors have explained regarding the multi-modal pore network that evolves during hydration [12,13]. Test 4, which reaches a slightly lower final degree of saturation (82.8%), presents a substantial decrease in total vertical stress due to the sample's macroporosity reduction (collapse). On the other hand, Test 5 reached a higher swelling pressure at a higher final degree of saturation (89.6%).

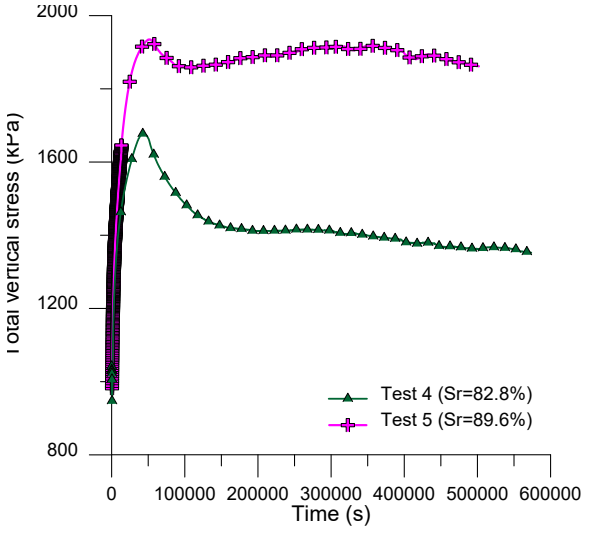

Fig. 6. Vertical stress evolution during hydration at constant volume.

Figure 7 shows the evolutions of absolute gas pressures starting at (1.00±0.15) MPa and at different initial total vertical stresses. An evident influence of the degree of saturation is observed on the absolute gas pressure decay curve, displaying a consistent decrease in the gas permeability with an increasing degree of saturation. Full dissipation of the absolute pressure was recorded after 300 s in Tests 3 and 4. However, Test 5, with a degree of saturation close to 90%, presents complete dissipation after 600 s. As expected, the complete dissipation reached the absolute atmospheric pressure (101 kPa).

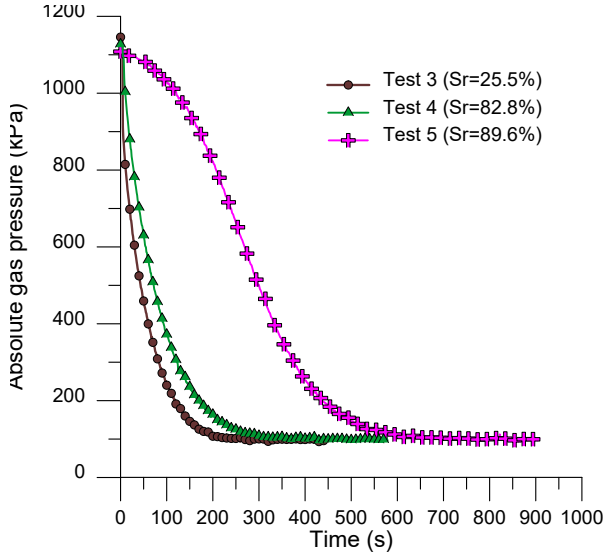

Fig. 7. Time evolution of gas pressure decay at different degrees of saturation.

4.4 Gas and water permeability results

Figure 8 presents the results of the effective gas permeability and the intrinsic water permeability after prolonged saturation (i.e., with a relative water permeability of one) obtained in stage 2 (Test 2). The legend of the figure presents the different results obtained. Tests 1 and 3 at similar initial conditions and low degree of saturation (around 27%) displayed approximately the same value of effective gas permeability ((2.36±0.01)×10^{-14} m^2). Test 4 at S_r=82.8% reached a somewhat lower value (1.67×10^{-14} m^2), but slightly higher than Test 5 (6.76×10^{-15} m^2 at S_r=89.6%). As observed, up to a relatively high degree of saturation of about 90%, the mixture displays a high and approximately constant effective gas permeability associated with the relatively high macro-porosity. Only after a nearly saturated state the connectivity of gas pathways is reduced, and the effective permeability drastically decreases to 2.50×10^{-20} m^2. At this saturation state (only gas pathways are desaturated), the effective permeability when transferring gas is slightly higher than when water flows (intrinsic permeability of 1.17×10^{-20} m^2). The observed differences in water and gas permeabilities can be associated with the fact that gas flows through different localised unsaturated pathways compared to the ones followed by water. In addition, differences could also be explained because of the pore pressure dependence on gas permeability of the Klinkenberg slippage effect, which is relevant when the intrinsic permeability is low (below 10^{-18} m^2) [14].

The current results of effective gas permeability were compared with data reported by [8] on a sand/bentonite mixture (80% quartz sand and 20% Kunigel V1 sodium bentonite) at a lower void ratio between e=0.40 and 0.60. As shown in Figure 8, at low degrees of saturation (< 50%) and despite the different void ratios, both mixtures display the same effective gas permeability. Nevertheless, at degrees of saturation > 70%, the sand/bentonite displays a lower ability of gas to flow, probably associated with the lower void ratio, and the stress paths followed (in the pellet/powder mixture, the decrease is evident at S_r > 90%). In the case of the sand/bentonite, the mixture was progressively wetted and then dried under constant vertical stress.

Test results (pellet/powder and sand/bentonite) have been fitted to a modified version of the expressions proposed by [8] based on a modified Kozeny-Carman equation for the effective gas permeability, which considers changes in the degree of saturation and the macrovoid ratio $e_M = e - e_m$. e_m represents the microvoid ratio associated with the void ratio inside intra-aggregate pores in powder and pellets. The following expressions have been used:

$$\frac{e_M}{e} = 1-(\alpha+\beta S_r)\ ;\ \alpha+\beta S_r \le 1$$
$$K_{eff} = \left[1-\left(\frac{S_r-\alpha}{1-\alpha}\right)^5\right]\left[A\frac{e_M^3}{1+e_M}\right] \quad (2)$$

where α and β are microstructural parameters accounting for the expansion of the intra-aggregate pores with the degree of saturation. α is associated with the shrinkage limit of the microstructure.

The fitted curve is presented in Figure 8. Fitted parameters are summarised in Table 2.

Table 2. Fitted parameters (Equation (2)).

Parameter	Degree of saturation (%)
α	0.20
β	0.50
A (m^2)	20×10^{-14}

To assess the effects of the microstructure's expansion and the inter-grain porosity's clogging, Figure 9 summarises effective gas permeability versus the percentage of bentonite filling of the inter-grain skeleton. Results for the sand/bentonite mixture have been based on data reported by [8]. Considering a granular powder dry density of 1.10 Mg/m^3, [7] estimated a volumetric degree of powder filling of F=61%. Under full saturation, powder filling the inter-pellet volume is assumed F=100%. The figure shows a good agreement between the different mixtures at several volumetric fillings, despite being prepared at various void ratios.

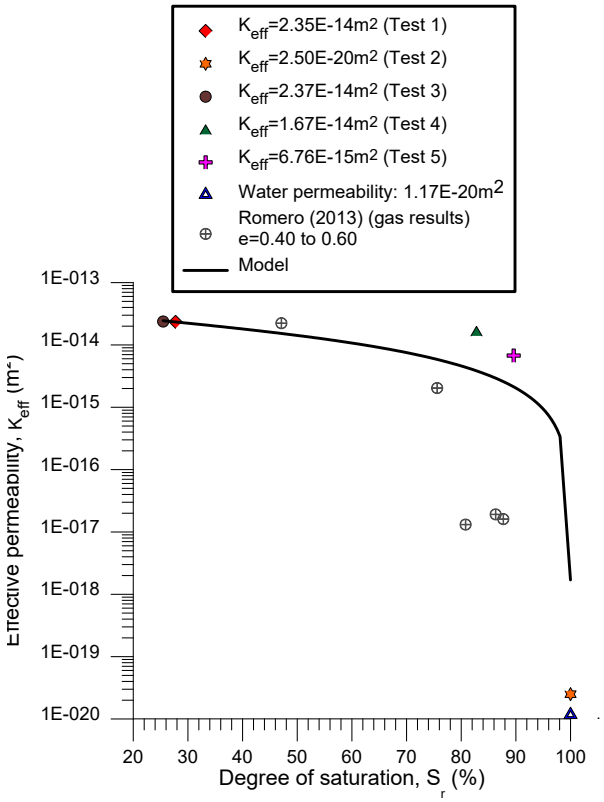

Fig. 8. Effective gas permeability versus degree of saturation.

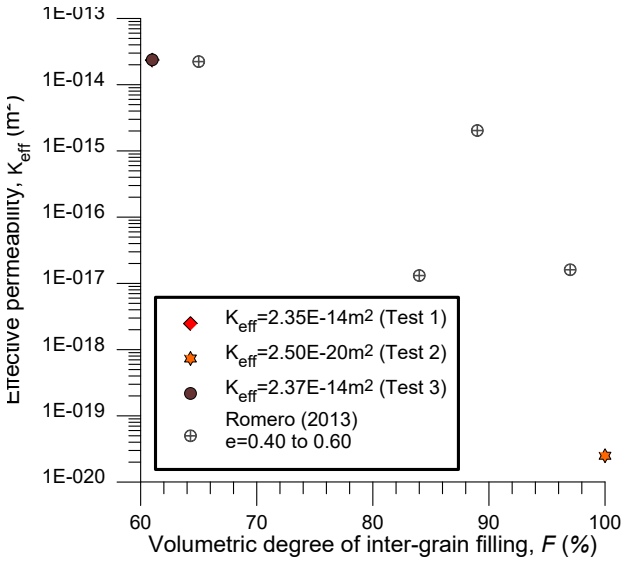

Fig. 9. Effective gas permeability versus degree of powder filling.

5 Concluding remarks

The paper presented an experimental study on the effective gas permeability of an MX80-type bentonite pellet/powder mixture (80% in mass of pellets), focusing on the effects of the degree of saturation and the estimation of the gas breakthrough pressure after saturation. At low degrees of saturation, the effective gas permeability reached 2.4×10^{-20} m². Nevertheless, the ability of gas to flow in the presence of liquid significantly reduced at degrees of saturation higher than 90%. The gas breakthrough pressure resulted in 1.5 MPa after allowing the sample to expand around 1% under oedometer conditions. The effective gas permeability during dissipation (unsaturated localised gas pathways) reached 2.50×10^{-20} m² (close to the intrinsic permeability of water). The effective gas permeability results were fitted to a modified Kozeny-Carman equation, which considered the degree of saturation and the macrovoid ratio (affected by the expansion of bentonite aggregates). These gas transport results were compared with published sand/bentonite mixtures data focusing on the volumetric filling of the inter-pellet or inter-grain porosity.

The authors acknowledge the financial support of 'Institut de Radioprotection et de Sûreté Nucléaire' IRSN (France) through a research project with the 'International Centre for Numerical Methods in Engineering' CIMNE (Spain).

References

1. N. Mokni, A. Molinero-Guerra, Y.-J. Cui, P. Delage, P. Aimedieu, M. Bornert, and A. M. Tang, Géotechnique **70**, 563 (2019).

2. A. Molinero-Guerra, N. Mokni, P. Delage, Y.-J. Cui, A. M. Tang, P. Aimedieu, F. Bernier, and M. Bornert, Appl. Clay Sci. **135**, 538 (2016).

3. J. F. Harrington, C. C. Graham, R. J. Cuss, and S. Norris, Appl. Clay Sci. **147**, 80 (2017).

4. P. Marschall, S. T. Horseman, and T. Gimmi, Oil Gas Sci. Technol. **60**, 121 (2005).

5. S. Saba, J.-D. Barnichon, Y.-J. Cui, A. M. Tang, and P. Delage, J. Rock Mech. Geotech. Eng. **6**, 126 (2014).

6. A. Mesa-Alcantara, Hydro-Mechanical Behaviour of Pellet / Powder Mixture of Bentonite and Impact of Gas Migration. Doctoral Thesis., Universitat Politècnica de Catalunya, 2021.

7. A. Mesa-Alcantara, E. Romero, N. Mokni, and S. Olivella, in *4th Eur. Conf. Unsaturated Soils (E-UNSAT 2020)* (Lisboa, Portugal, 2020), p. 04003.

8. E. Romero, Eng. Geol. **165**, 3 (2013).

9. A. Mesa-Alcantara, N. Mokni, E. Romero, and S. Olivella, in *4th Eur. Conf. Unsaturated Soils (E-UNSAT 2020)* (Lisboa, Portugal, 2020), p. 04004.

10. L. Gonzalez-Blanco, E. Romero, and P. Marschall, in *4th Eur. Conf. Unsaturated Soils (E-UNSAT 2020)* (2020), p. 04008.

11. L. Gonzalez-Blanco, E. Romero, C. Jommi, X. Sillen, and X. Li, Adv. Lab. Test. Model. Soils Shales. Springer, Cham 288 (2017).

12. A. Gens, M. Sánchez, B. Valleján, C. Imbert, M. V. Villar, and M. Van Geet, Géotechnique **61**, 367 (2011).

13. C. Imbert and M. V. Villar, Appl. Clay Sci. **32**, 197 (2006).

14. R. W. Zimmerman, *Imperial College Lectures In Petroleum Engineering, The-Volume 5: Fluid Flow In Porous Media* (World Scientific, 2018).